Further Development and Optimization of the MR-FDPF Algorithm

D1.1: Progress Report

Dmitry Umansky, Jean-Marie Gorce, Guillaume Villemaud

March 4, 2011

Abstract

Radio propagation tools are needed to help operators to find the best setting of their network, including but not limited to access points positioning, radiated power optimization, and channel selection. Hence, different approaches proposed in the literature deal with this issue. Empirical models suffer from an unacceptable lack of accuracy while deterministic models have to cope with exponential computational complexity. Geometric models like ray tracing [1], [2] have been extensively developed as they offer a good trade-off between computational load and accuracy but they fail in simulating properly severe environments where multiple diffractions and numerous reflections hold. Second, more accurate methods based on the resolution of the Maxwells equations have been implemented [3], [4] but they suffer from a high computational load. The Multi-Resolution Frequency Domain Partial Flows (MR-FDPF) approach [5] was proposed to fill in the gap by developing a multi-resolution preprocessing for the frequency domain Transmission-Line Modeling (TLM) approach.

The objective of this document is to present the results related to further development and optimization of the MR-FDPF method. Two feasibility studies that have been recently conducted are reported here. First, the possibility of applying the MR-FDPF approach to simulating the Orthogonal Frequency-Division Multiplexing (OFDM) and the multiple-input multiple-output (MIMO) systems has been examined. In the second feasibility study, we have considered the application of the multi-resolution frequency-domain (MR-FD) approach to the TLM method in order to efficiently simulate the radio wave propagation in 3D indoor environments.

1 Introduction

As an introduction, we provide the necessary background on the MR-FDPF approach. The early version of the MR-FDPF method has been derived for indoor like environments [6, 7] but we also proved in [8] that it can be extended is some cases to large urban scales, if a fake simulation frequency is used. From our opinion however, the major interest of the method is when hard propagation conditions occur such as in Indoor. As described in an associated paper [9], we guess that coupling MR-FDPF with a ray-tracer is the most promising issue for large scale simulations.

The initial ParFlow method relies on a TLM like formalism [10]. Flows are defined on edges between nodes in a regular grid. The waves propagate along the edges and transmissions and reflections are tuned with linear equations that are associated with each node. From a general point of view, this system can be expressed under a general matrix equation:

$$F(t + dt) = W \cdot F(t) + S(t) \tag{1}$$

where F(t) is a state vector that contains all propagating flows on the edges, and S(t) is the source vector. The matrix M is the transmission matrix. In the frequency domain, the steady-state problem turns into a linear system according to:

$$(I_d - W) \cdot F = S \tag{2}$$

where I_d refers to the identity matrix, and F to the harmonic flows vector. We showed previously how this system can be solved in a recursive manner, exploiting a recursive dividing procedure as represented in Fig.1. In practice,

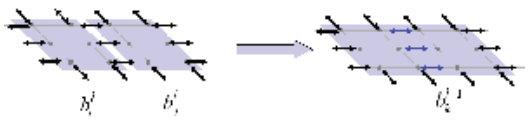

Figure 1: father and children node flows are related with linear operations in steady-state

MR-FDPF approach runs in two steps:

- During the first step, 'vertical' propagation matrices are recursively computed. These matrices allow to update boundary flows from children nodes to father and inversely. The computational cost of this part is the highest part and is in $O(n^3)$ [6] but the interesting property is that this preprocessing is node once whatever the source position. This computational complexity order is further identical to that of computing the coverage of one source with a time domain implementation.
- During the second step, the propagation is performed 'vertically' in the multi-resolution structure. This phase exhibits the advantages of the method: the computational load is only in $O(n^2)$ per source and the exact steady-state result is obtained while all propagation paths are accounted for. In addition, the descending propagation process can be stopped at a certain block size, and statistic parameters can be estimated from inward flows as illustrated in Fig.2.

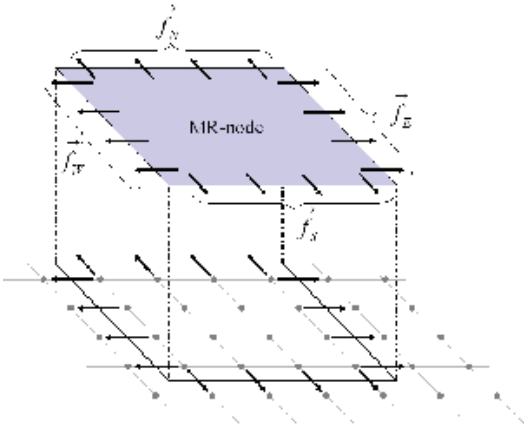

Figure 2: This figure represents a block with inward flows from which local statistics can be derived.

2 On Simulating Propagation for OFDM/MIMO Systems with the MR-FDPF Model

Last years, a technological shift in wireless communications has been observed. After few years with a major interest on direct spreading and CDMA based radio access technologies, OFDMA and MIMO are the two key technologies exploited everywhere especially in Indoor like environments [11]. The former successfully exploits frequency diversity while the later exploits spatial diversity. These two technologies all together allow approaching the Shannon's capacity limit, even in strong fading conditions. However, the practical capacity of these networks is not known yet for two main reasons: First, the optimal bound can be approximated only if the transmitter exploits a feedback channel to obtain good channel state information . Second, as wireless networks are densely deployed, interference plays a crucial role. Predicting and managing interference locally while achieving a global optimization is still an open problem [12–14]. Simulations and models are very important to validate distributed algorithms for resource allocation, but classical signal strength predictions are not sufficient. A system level simulation is much more complex because some signal features are needed. This question arises especially when MIMO and OFDM are used because they require a very fine resolution in space and frequency domains respectively. It is obviously impossible to derive an exact determinist approach as many uncertainties are present in complex environments. It is therefore more significant to predict some statistical parameters in addition to the classical signal strength. Practically speaking, frequency, spatial and time statistics are needed. Concerning OFDM, the bandwidth is divided in several sub-channels, each one having its own channel response h_i. To evaluate OFDM transmission performance, three kinds of information are mandatory: (i) the average channel gain, (ii) the channel statistics, and (iii) the sub-channels intercorrelation. Average channel gains are predictable with classical simulation approaches but the channel statistics are more difficult to obtain. The objective is for instance to determine the Rice parameter (if the channel is Ricean). This problem was

investigated in [15]. However the extension to the case of wideband systems may generate a high computational load. Concerning MIMO, the system level performance still relies on predicting the same three components. But the channels are now spatially distributed. A deterministic simulation cannot predict accurately the difference between two antennas separated from only few centimeters. Still, a statistical approach is preferred to derive an estimation of the inter-channel correlation strength.

As detailed in [6], the MR-FDPF approach was designed for simulating radio coverage maps from steady-state simulations. At a first glance, this approach seems adequate neither for wideband systems nor for MIMO systems. Albeit, we will discuss in the following how this method can be adapted to this context. Further, some specific features of MR-FDPF reveal to be even very powerful.

2.1 Statistic estimations

The MR-FDPF method provides a sub-wavelength resolution. The simulations are extremely fine but strictly not exact since many artifacts in the real world are not taken into account and affect the exact value of the predicted field. Such a fine estimation is however very interesting to estimate local statistics because it provides a possible picture of what the field could be in any area. For example, we presented in [15], a study on signal strength statistics in some blocks and comparison with measurements exhibited a good agreement. The principle was to measure signal strength variations in a free-space block as represented in Fig.2. From a given block, for which the inward flows have been estimated from the rest of the environment, we can proceed to a local analysis of the incoming flows because they are directly related to the fied values inside the block. In a block, the incoming flows allow to characterize the complete field inside.

$$\Psi = W_d \cdot F_{in} \tag{3}$$

where F_{in} is the vector of incoming flows, Ψ the vector field containing all field in the block and W_d is the downward matrix. Thus, the field values are obtained by linear combinations of the incoming flows. In a block, the first meaningful parameter is the average SNR, proportional to the average received power $\bar{\Gamma} = \langle |\Psi|^2 \rangle$ easily derived as:

$$\bar{\Gamma} = \frac{1}{N_x \cdot N_y} F_{in}^{\perp} \cdot W_d^{\perp} \cdot W_d \cdot F_{in} \tag{4}$$

where N_x and N_y are the block dimensions. Let be considered the standard value decomposition (SVD) $W_d = U^{\perp} \Sigma V$ where U and V are unitary matrices and Σ is a diagonal matrix. Note that we have also $W_d^{\perp} W_d = V^{\perp} \cdot \Lambda \cdot V$, wigth $\Lambda = \Sigma^{\perp} \cdot \Sigma$. Then, the inward flows can be projected in the eigenspace $G_{in} = V \cdot F_{in}$ leading to a very efficient computation of the average power in a block:

$$\bar{\Gamma} = \frac{1}{N_x \cdot N_y} G_{in}^{\perp} \cdot \Lambda \cdot G_{in} \tag{5}$$

The SVD decomposition is also very interesting to determine the main mode of the block, i.e. the inward flows that penetrate the most efficiently in the block. Indeed, the inward flow vector aligned to the highest singular value corresponds to the most efficient solution. However, the SVD decomposition cannot be used

directly for computing higher order moments and the mean amplitude field. In [15], we explained how the fading strength can be estimated with the k parameter from the first and second moments of the envelope distribution. The envelope first moment A is given by:

$$\bar{A} = \frac{1}{N_x \cdot N_y} \sum_j |\Psi(j)| = \frac{1}{N_x \cdot N_y} \sum_j |u_j \cdot \Sigma \cdot G_{in}| \tag{6}$$

where u_i is the i^{th} eigen vector of U. Then, according to [15] the fading parameter is estimated with:

$$k = \frac{\sqrt{1 - \frac{\Gamma - \bar{A}^2}{\Gamma^2}}}{1 - \sqrt{1 - \frac{\Gamma - \bar{A}^2}{\Gamma^2}}} \tag{7}$$

2.2 MIMO channel predictions

MIMO systems are now very usual in high rate wireless communications [11, 16]. They proved being very efficient in many context especially in Indoor like environment as they increase the diversity degree of radio links. However, the MIMO gain depends on the fading strength and inter-channel correlation [17]. The fading strength of each channel can be estimated as described above, while the intercorrelation can be characterized with the intercorrelation matrix defined as:

$$R_{hh} = E\langle h.h^{\perp} \rangle \tag{8}$$

where h is the steady-state channel vector. Predicting this correlation is a hard issue in simulation as wide and short scale phenomnon have to be considered simultaneously because the different antennas are put together in a very close space. we know discuss how MR-FDP offers a good framework for such task.

2.2.1 Integration in MR-FDPF

To obtain a simple but efficient approach we use the matricial nature of the MR-FDPF engine. Let a transmitter be located in a block B_s and a receiver in a boc B_r. In MR-FDPF, directive radiation patterns can be generated with a set of multiple point source fitting with a reference radiation pattern $r(\theta)$ [18]:

$$r(\theta) = \sum_{k \in B_s} s_k \cdot e^{-j\beta\delta(k,\theta)} \tag{9}$$

where $s_k; k \in B_s$ correspond to the complex values of the equivalent sources in the k^{th} point in B_s. Then, the source beamforming vector $V_b(s) = \{s_k; k \in B_s\}$ is derived from the discretized radiation pattern Z_θ in association with a smoothing constraint represented by a matrix Sm, leading to :

$$V_b(s) = \frac{H^{\perp}}{H^{\perp}H + \mu Sm} Z_\theta \tag{10}$$

Whatever the radiation pattern, the same radiated field can be also obtained from the boundary outgoing flows of B_s, noted $F_{out}(s)$ and defined by :

$$F_{out}(s) = W_u \cdot V_b(s) \cdot S_0 \tag{11}$$

where W_u is the reverse matrix of W_d and S_0 is the complex coefficient of the source.

Let us now switch to the receiver block. Thanks to the reciprocity theorem, the beamforming vector in reception can be derived in a similar way, allowing to express the received field by using the beamforming vector (10) of the receiving antenna:

$$\Psi = V_b(r)^{\perp} \cdot \Psi(d) \tag{12}$$

where $\Psi(d)$ is the field vector in the block B. As above, we can also simplify the computation by exploiting the linear relation between boundary incoming flows and filed values leading to:

$$\Psi = V_b(r)^{\perp} \cdot W_d \cdot F_{in}(d) \tag{13}$$

Then, MIMO simulations can be derived by exploiting (11) and (13) and defining different beamforming vectors for transmission and reception $V_S = \{V_{b1}(s), V_{b2}(s), \ldots, V_{bN}(s)\}$ and $V_R = \{V_{b1}(r), V_{b2}(r), \ldots, V_{bN}(r)\}$ respectively. To compute the correlation matrix with (8), the expectation requires different realization. We propose to use a wide set of beamforming antennas, and the expectation can be performed over random selections of antennas in these sets. To avoid a high increase of the computational load, each outgoing flow from s, $f_k(s)$ is propagated solely in the multi-resolution structure to obtain the incoming flows in the destination block. Then, the linear relationship between the source and destination flows are obtained by the propagation matrix $W_P(s, d)$ which relates each source flow to each destination flow:

$$F_{in}(d) = W_P(s, d) \cdot F_{out}(s) \tag{14}$$

Therefore, the computational complexity of this approach is independent on the beamforming vectors set, but only proportional to the source block size. This approach allows to simulate partially correlated MIMO channels that take into account the real environment.

2.3 Wideband predictions

2.3.1 Wideband characteristics

In, OFDMA, the bandwidth is subdivided into sub-channels [13, 19]. The fading in each sub-channel is supposed flat and therefore the carrier spacing represents the maximal frequency resolution required for measuring the frequency response. In practice however, this resolution is often much fine than the experimental frequency correlation, and in practice, several adjacent channels are affected with a correlated fading. In 802.11a for instance, the channel width of $20MHz$ is divided into 52 sub-channels spacing with a carrier spacing equal to $312.5kHz$. Full resolution frequency response estimation would require 52 samples. The optimal frequency resolution can be also estimated from the channel time spreading with $\Delta f < 1/T_s$ where T_s is the channel time spreading. In usual Indoor environments, time spreading is in the order of few hundred nanoseconds around $2.4GHz$. This led us considering a frequency resolution of $1MHz$. A full bandwidth estimation of the frequency response thus needs about 20 samples in the frequency domain.

From such simulation, we need a statistical estimation of the channel characteristics. The fading strength is still important for each sub-channel, but the frequency channels inter-correlation is of primary importance. Let us note h_j, the channel associated with carrier j,and $h = [h_j]^t$, the channel vector. The inter-correlation can be represented with the correlation matrix defined in (8), where the channel coefficients h_i now correspond to the frequency carriers.

2.3.2 Implementation in MR-FDPF

Wideband simulation is a very challenging issue for MR-FDPF since this approach is based on a steady-state study. Therefore, the complete propagation mechanism detailed in section II should be done several times. The main drawback of this approach is that the high computational load of the pre-processing phase is repeated as many times as the number of independent carriers. Therefore, the main limit for this wideband approach is related to the need of developing the whole preprocessing for each carrier frequency. This generates a large computational overload but also a large increase of memory resource needs, since all vertical propagation matrices have to be stored and maintained in the random access memory. if the bandwidth is very small compared to the carrier frequency, an approximated computation may appear efficient. Let us note the solution at the central frequency:

$$F(f_0) = (I_d - W(f_0))^{-1} \cdot S \tag{15}$$

where $W(f_0)$ is the propagation matrix, noted W_0 in the following. The same expression can be derived for another frequency $f_0 + \Delta f$ according to:

$$F(f_0 + \Delta f) = (I_d - W(f_0 + \Delta f))^{-1} \cdot S \tag{16}$$

Note that $W(f_0 + \Delta f) = e^{(-j2\pi\Delta f \Delta t)} W(f_0)$. The time interval Δt is equal to $dr/(\sqrt{2}c)$ where dr denotes the distance between the neighboring nodes and c is the speed of light. We can rewrite (16) as:

$$F(f_0 + \delta_f) = \left(I_d - W(f_0) + W(f_0) - e^{-j2\pi\Delta f \Delta t} W(f_0)\right)^{-1} \cdot S \tag{17}$$

Now, introducing $F(f_0)$ into (17) provides:

$$F(f_0 + \delta_f) = \left(I_d - (Id - W(f_0))^{-1} \cdot W_{\delta f}\right)^{-1} \cdot F(f_0) \tag{18}$$

where $W_{\delta f} = (e^{-j2\pi\Delta f \Delta t} - 1) \cdot W(f_0)$. Using the Neumann series we write:

$$\begin{aligned} F(f_0 + \delta_f) = \big(I_d + (Id - W(f_0))^{-1} \cdot W_{\delta f} + \\ \left((Id - W(f_0))^{-1} \cdot W_{\delta f}\right)^2 + \dots\Big) \cdot F(f_0) \end{aligned} \tag{19}$$

At first order, one obtain:

$$F(f_0 + \delta_f) \approx F(f_0) + F^{(1)}(\delta f) \tag{20}$$

with

$$F^{(1)}(\delta f) = (Id - W(f_0))^{-1} \cdot W_{\delta f} \cdot F(f_0) \tag{21}$$

This approach is very promising as it becomes possible to compute and keep in memory the matrices computed for a unique frequency. Further, the computational overload for the propagation phase is acceptable. The solution flows at f_0 are used as sources, then propagated locally to their first neighbors with $W_{\delta f}$ and finally propagated vertically in the multi-resolution structure over the whole space. If the first order approximation appears not sufficient, a second order approximation can be assessed by adding a third term equal to

$$F^{(2)}(\delta f) = (Id - W(f_0))^{-1} \cdot W_{\delta f} \cdot F^{(1)}(\delta f) \tag{22}$$

which can be generalized to higher order terms:

$$F^{(n+1)}(\delta f) = (Id - W(f_0))^{-1} \cdot W_{\delta f} \cdot F^{(n)}(\delta f) \tag{23}$$

At each step, the computational cost is constant.

3 The MR-FD Implementation of the TLM Method for Simulating Radio Wave Propagation in 3D Space

The MR-FD ParFlow (MR-FDPF) algorithm has proved to be a computationally efficient method for simulating radio wave propagation in 2D indoor environments [5]. The MR-FDPF method is based on the Lattice-Boltzmann (LB) approach formulated, e.g., in [20]. In the LB model for simulating wave propagation in 2D space, each point of the lattice is represented by the scattering matrix. Similar representation of the propagation medium, i.e., by means of the scattering matrix defined for each node of the mesh, can be found in the well-known TLM method see, e.g., [21]. In contrast to the LB approach, which cannot be readily extended to simulate wave propagation in 3D space, the 3D TLM method is available. Thus, it is of interest to investigate if the MR-FD implementation of the 3D TLM method can be found. If such implementation, which in the following will be referred as 3D MR-FDTLM, exists, then its computational efficiency can be compared to that of a more traditional time-domain realizations of the 3D TLM method.

3.1 The 3D TLM Symmetrical Super-Condensed Node

In the TLM method, the wave propagation environment is modeled as an aggregation of transmission lines interconnected at nodes. In 3D space, the nodes are constructed by interconnecting 12 transmission lines and up to 6 stubs [22]. The stubs are introduced into the nodes to allow modeling of inhomogeneous propagation media on a graded mesh.

However, it has been demonstrated in [22] that the presence of the stubs in the nodes can be totally avoided. The nodes constructed by interconnecting only the transmission lines are called symmetrical supper-condensed nodes (SSCNs). In the rest of this section, we briefly describe some of the important features of the SSCNs. A more detailed description of the SSCNs can be found in [22].

3.1.1 Scattering Matrix

Below, the incident and reflected voltage pulses traveling along a particular transmission line are denoted by the superscripts i and r, respectively. The scattering equation reads as

$$\mathbf{v}^r = \mathbf{S}\mathbf{v}^i \tag{24}$$

where $\mathbf{v}^i = [v^i_{ynx} v^i_{znx} v^i_{xny} v^i_{zny} v^i_{ynz} v^i_{xnz} v^i_{ypz} v^i_{zpy} v^i_{zpx} v^i_{xpz} v^i_{xpy} v^i_{ypx}]^T$ and $\mathbf{v}^r = [v^r_{ynx} v^r_{znx} v^r_{xny} v^r_{zny} v^r_{ynz} v^r_{xnz} v^r_{ypz} v^r_{zpy} v^r_{zpx} v^r_{xpz} v^r_{xpy} v^r_{ypx}]^T$ (see Fig. 3).

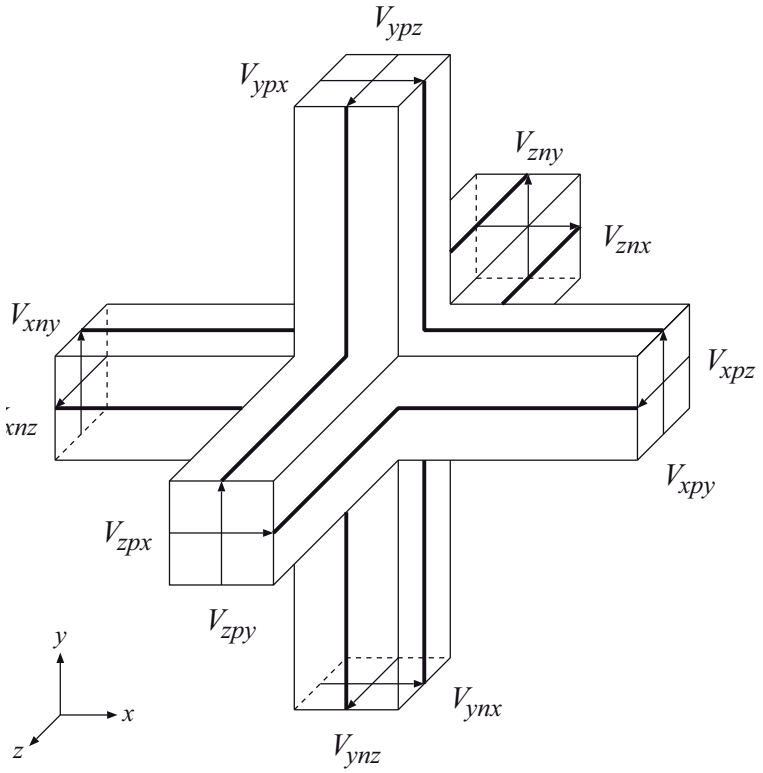

Figure 3: The 3D TLM symmetrical super-condensed node.

The scattering matrix of the SSCN is given by

$$\mathbf{S} = \begin{bmatrix}
a_{yx} & b_{yx} & d_{yx} & 0 & 0 & 0 & 0 & 0 & b_{yx} & 0 & -d_{yx} & c_{yx} \\
b_{zx} & a_{zx} & 0 & 0 & 0 & d_{zx} & 0 & 0 & c_{zx} & -d_{zx} & 0 & b_{zx} \\
d_{xy} & 0 & a_{xy} & b_{xy} & 0 & 0 & 0 & b_{xy} & 0 & 0 & c_{xy} & -d_{xy} \\
0 & 0 & b_{zy} & a_{zy} & d_{zy} & 0 & -d_{zy} & c_{zy} & 0 & 0 & b_{zy} & 0 \\
0 & 0 & 0 & d_{yz} & a_{yz} & b_{yz} & c_{yz} & -d_{yz} & 0 & b_{yz} & 0 & 0 \\
0 & d_{xz} & 0 & 0 & b_{xz} & a_{xz} & b_{xz} & 0 & -d_{xz} & c_{xz} & 0 & 0 \\
0 & 0 & 0 & -d_{yz} & c_{yz} & b_{yz} & a_{yz} & d_{yz} & 0 & b_{yz} & 0 & 0 \\
0 & 0 & b_{zy} & c_{zy} & -d_{zy} & 0 & d_{zy} & a_{zy} & 0 & 0 & b_{zy} & 0 \\
b_{zx} & c_{zx} & 0 & 0 & 0 & -d_{zx} & 0 & 0 & a_{zx} & d_{zx} & 0 & b_{zx} \\
0 & -d_{xz} & 0 & 0 & b_{xz} & c_{xz} & b_{xz} & 0 & d_{xz} & a_{xz} & 0 & 0 \\
-d_{xy} & 0 & c_{xy} & b_{xy} & 0 & 0 & 0 & b_{xy} & 0 & 0 & a_{xy} & d_{xy} \\
c_{yx} & b_{yx} & -d_{yx} & 0 & 0 & 0 & 0 & 0 & b_{yx} & 0 & d_{yx} & a_{yx}
\end{bmatrix} \tag{25}$$

where

$$\begin{aligned} a_{ij} &= Q_j - b_{ij} - d_{ij} \\ b_{ij} &= Q_j \hat{C}_{kj} \\ c_{ij} &= Q_j - b_{ij} + d_{ij} - 1 \\ d_{ij} &= P_k \hat{L}_{ij} \end{aligned} \tag{26}$$

and

$$\begin{aligned} \hat{C}_{kj} &= \frac{Y_{kj}}{Y_{ij} + Y_{kj}} = \frac{Z_{ij}}{Z_{ij} + Z_{kj}} \\ \hat{L}_{ij} &= \frac{Z_{ij}}{Z_{ij} + Z_{ji}} \\ Q_j &= \left(1 + \frac{G_{ej}}{2(Y_{ij} + Y_{kj})}\right)^{-1} \\ P_k &= \left(1 + \frac{R_{mk}}{2(Z_{ij} + Z_{ji})}\right)^{-1}. \end{aligned} \tag{27}$$

For a uniform mesh, i.e., $\triangle x = \triangle y = \triangle z = \triangle l$, and for isotropic media, the line impedances are defined in [22] according to

$$\begin{aligned} Z_{xy} = Z_{yz} = Z_{zx} = Z_p &= \left(\sqrt{\varepsilon_r \mu_r} \mp \sqrt{\varepsilon_r \mu_r - 1}\right) \sqrt{\frac{\mu}{\varepsilon}} \\ Z_{zy} = Z_{xz} = Z_{yx} = Z_n &= \left(\sqrt{\varepsilon_r \mu_r} \pm \sqrt{\varepsilon_r \mu_r - 1}\right) \sqrt{\frac{\mu}{\varepsilon}} \end{aligned} \tag{28}$$

where both signs are meaningful and either solution, i.e., corresponding to either upper $+$ or $-$, can be used.

Note that in Eq. (27), the parameters G_{ej} and R_{mj} signify, respectively, the electrical and magnetic losses, and are defined as

$$\begin{aligned} G_{ej} &= \sigma_e \triangle l \\ R_{mj} &= \sigma_m \triangle l \end{aligned} \tag{29}$$

where σ_e and σ_m are the electric and magnetic conductivities, respectively.

Due to the fact that the line impedance experiences a discontinuity at the interfaces between two nodes belonging to two different media, the partial reflections from the junction have to be taken into account while calculating the results of the scattering at the nodes.

3.1.2 Output

The components of the electric and the magnetic fields at each node can be calculated as follows

$$\begin{aligned} E_j &= -V_j / \triangle l \\ H_k &= I_k / \triangle l \end{aligned} \tag{30}$$

where

$$\begin{aligned} V_j &= 2\frac{Y_{ij}(v^i_{inj}+v^i_{ipj})+Y_{kj}(v^i_{knj}+v^i_{kpj})}{2Y_{ij}+2Y_{kj}+G_{ej}} \\ I_k &= 2\frac{v^i_{ipj}-v^i_{inj}+v^i_{jni}-v^i_{jpi}}{2Z_{ij}+2Z_{ji}+R_{mk}}. \end{aligned} \tag{31}$$

3.1.3 Excitation

To inject the electrical field component E_j into the mesh, the following voltage pulses need to be generated

$$\begin{aligned} v^i_{inj} &= v^i_{ipj} = \frac{-E_j\triangle l}{8}\frac{2Y_{ij}+2Y_{kj}+G_{ej}}{Y_{ij}} \\ v^i_{knj} &= v^i_{kpj} = \frac{-E_j\triangle l}{8}\frac{2Y_{ij}+2Y_{kj}+G_{ej}}{Y_{kj}}. \end{aligned} \tag{32}$$

Similarly, for injecting the magnetic field component H_k, the following voltage pulses are injected

$$v^i_{ipj} = -v^i_{inj} = v^i_{jni} = -v^i_{jpi} = \frac{H_k\triangle l}{8}(2Z_{ij}+2Z_{ji}+R_{mk}). \tag{33}$$

3.1.4 Computational Complexity

According to [22], modeling of lossy anisotropic propagation media requires 48 additions/subtractions and 6 multiplications per SSCN node per time step.

3.2 The MR-FDTLM Implementation

In the previous section, the properties of the SSCN developed in [22] have been summarized. The choice of the SSCN is mainly dictated by the absence of stubs, which means that the size of the scattering matrix can be noticeably reduced compared to the stub-loaded symmetrical condensed nodes (SCNs) and the hybrid nodes [22].

3.2.1 Scattering equation

Perhaps, the only impediment that prevents a direct application of the MR-FD approach to the TLM method is the reflections/transmissions happening at the interfaces between different node regions, i.e., at the boundaries between different propagation media. As it is shown below, this impediment can be removed.

The state-space representation of the scattering equation (24) can be written as

$$\begin{aligned} \mathbf{x}[(n+1)\triangle t] &= \mathbf{R}^p\mathbf{x}[n\triangle t]+\mathbf{S}^p\mathbf{v}^i[n\triangle t] \\ \mathbf{v}^r[n\triangle t] &= \mathbf{T}^p\mathbf{x}[n\triangle t]+\mathbf{s}^i[n\triangle t]. \end{aligned} \tag{34}$$

Here, the vector $\mathbf{s}^i[n\triangle t] = [s^i_{ynx}s^i_{znx}s^i_{xny}s^i_{zny}s^i_{ynz}s^i_{xnz}s^i_{ypz}s^i_{zpy}s^i_{zpx}s^i_{xpz}s^i_{xpy}s^i_{ypx}]^T$ denotes the excitation signal associated with a source. The elements of the vector $\mathbf{s}^i$ are calculated according to (32) or/and (33) (see Subsection **??**). The

vectors $\mathbf{v}^i$, $\mathbf{v}^r$, and the scattering matrix $\mathbf{S}$ have been defined in (24). The vector $\mathbf{x}$ represents the state variables. The superscript p shows association with the node p. Correspondingly, the superscript $p+1$ signifies a node neighboring the node p on any of its sides. The matrices $\mathbf{R}^p$ and $\mathbf{T}^p$ are diagonal.

The elements R^p_{ij}, $i,j \in \{x,y,z\}$, on the main diagonal of the reflection matrix $\mathbf{R}^p$ are given by

$$R^p_{ij} = \frac{Z^{p+1}_{ij} - Z^p_{ij}}{Z^{p+1}_{ij} + Z^p_{ij}}. \tag{35}$$

Note that when both nodes p and $p+1$ belong to the same medium, the corresponding element R^p_{ij} of the matrix $\mathbf{R}^p$ equals zero. Thus, if the node p is surrounded by the nodes of the same medium, the reflection matrix $\mathbf{R}^p$ is zero.

The diagonal elements T^p_{ij}, $i,j \in \{x,y,z\}$, of the transmission matrix $\mathbf{T}^p$ are defined as

$$T^p_{ij} = \frac{2Z^p_{ij}}{Z^{p+1}_{ij} + Z^p_{ij}}. \tag{36}$$

When both nodes p and $p+1$ belong to the same medium, the corresponding element T^p_{ij} of the matrix $\mathbf{T}^p$ is 1. Thus, the transmission matrix $\mathbf{T}^p$ becomes the identity matrix $\mathbf{I}$, when the node p is surrounded by the nodes of the same medium.

By taking the Fourier transform of (34) and after straightforward manipulations we can obtain

$$\begin{aligned} \mathbf{v}^r(f) &= \mathbf{T}^p \left(\mathbf{I} - \mathbf{R}^p e^{-j2\pi f \triangle t}\right)^{-1} e^{-j2\pi f \triangle t} \mathbf{S}^p \mathbf{v}^i(f) + \mathbf{s}^i(f) \\ &= \mathbf{W}^p(f)\mathbf{v}^i(f) + \mathbf{s}^i(f) \end{aligned} \tag{37}$$

which is similar to the frequency domain ParFlow formulation given in [5].

3.2.2 External boundaries

Equation (37) also allows simulating external boundaries of arbitrary reflection coefficient ρ. For this case, the diagonal elements R^p_{ij} of the reflection matrix $\mathbf{R}^p$ are calculated according to (see [22])

$$R^p_{ij} = \frac{\sqrt{\mu/\varepsilon}(1+\rho) - Z_{ij}(1-\rho)}{\sqrt{\mu/\varepsilon}(1+\rho) + Z_{ij}(1-\rho)}. \tag{38}$$

3.2.3 Composition of scattering blocks

Similar to the scattering equation (37), which describes the relationship between the the incident and reflected voltages for a single SSCN node, we can write the scattering equation for the block of nodes A

$$\mathbf{v}^r_A = \mathbf{W}_A \mathbf{v}^i_A + \mathbf{s}^i_A. \tag{39}$$

where the excitation signals aggregated in the vector $\mathbf{s}^i_A$ correspond to all sources located inside the block A. Although omitted for simplifying the notation in (39), the dependence on frequency is understood.

Suppose the block A and the block B are connected by k lines. Then, the scattering equations (39) can be written for the blocks A and B as follows (see also [23])

$$\begin{bmatrix} \mathbf{W}_{A_{11}} & \mathbf{W}_{A_{12}} \\ \mathbf{W}_{A_{21}} & \mathbf{W}_{A_{22}} \end{bmatrix} \begin{bmatrix} \mathbf{v}^i_{A_1} \\ \mathbf{v}^i_{A_2} \end{bmatrix} + \begin{bmatrix} \mathbf{s}^i_{A_1} \\ \mathbf{s}^i_{A_2} \end{bmatrix} = \begin{bmatrix} \mathbf{v}^r_{A_1} \\ \mathbf{v}^r_{A_2} \end{bmatrix}, \quad \begin{matrix} \} \\ \} \end{matrix} \begin{matrix} N_A - k \\ k \end{matrix}$$
$$\begin{bmatrix} \mathbf{W}_{B_{11}} & \mathbf{W}_{B_{12}} \\ \mathbf{W}_{B_{21}} & \mathbf{W}_{B_{22}} \end{bmatrix} \begin{bmatrix} \mathbf{v}^i_{B_1} \\ \mathbf{v}^i_{B_2} \end{bmatrix} + \begin{bmatrix} \mathbf{s}^i_{B_1} \\ \mathbf{s}^i_{B_2} \end{bmatrix} = \begin{bmatrix} \mathbf{v}^r_{B_1} \\ \mathbf{v}^r_{B_2} \end{bmatrix}, \quad \begin{matrix} \} \\ \} \end{matrix} \begin{matrix} N_B - k \\ k \end{matrix} \tag{40}$$

where the subvectors $\mathbf{v}^i_{A_2}$, $\mathbf{v}^r_{A_2}$, $\mathbf{v}^i_{B_2}$, and $\mathbf{v}^r_{B_2}$, which correspond to the k lines connecting the blocks A and B, are related as

$$\mathbf{v}^i_{A_2} = \mathbf{v}^r_{B_2} \qquad \mathbf{v}^r_{A_2} = \mathbf{v}^i_{B_2}. \tag{41}$$

Note that in general, the size N_A of the scattering matrix $\mathbf{W}_A$ can be different from the size N_B of the scattering matrix $\mathbf{W}_B$. Using (41), we obtained from (40)

$$\begin{aligned} \mathbf{W}_{A_{22}}\mathbf{v}^i_{A_2} - \mathbf{v}^i_{B_2} &= -\mathbf{W}_{A_{21}}\mathbf{v}^i_{A_1} - \mathbf{s}^i_{A_2} \\ \mathbf{v}^i_{A_2} - \mathbf{W}_{B_{22}}\mathbf{v}^i_{B_2} &= -\mathbf{W}_{B_{21}}\mathbf{v}^i_{B_1} - \mathbf{s}^i_{B_2} \end{aligned} \tag{42}$$

and consequently

$$\begin{aligned} \mathbf{v}^i_{A_2} &= \left(\mathbf{I} - \mathbf{W}_{B_{22}}\mathbf{W}_{A_{22}}\right)^{-1} \left(\mathbf{W}_{B_{21}}\mathbf{v}^i_{B_1} + \mathbf{W}_{B_{22}}\mathbf{W}_{A_{21}}\mathbf{v}^i_{A_1}\right) + \\ &+ \left(\mathbf{I} - \mathbf{W}_{B_{22}}\mathbf{W}_{A_{22}}\right)^{-1} \left(\mathbf{s}^i_{B_2} + \mathbf{W}_{B_{22}}\mathbf{s}^i_{A_2}\right) \\ \mathbf{v}^i_{B_2} &= \left(\mathbf{I} - \mathbf{W}_{A_{22}}\mathbf{W}_{B_{22}}\right)^{-1} \left(\mathbf{W}_{A_{21}}\mathbf{v}^i_{A_1} + \mathbf{W}_{A_{22}}\mathbf{W}_{B_{21}}\mathbf{v}^i_{B_1}\right) + \\ &+ \left(\mathbf{I} - \mathbf{W}_{A_{22}}\mathbf{W}_{B_{22}}\right)^{-1} \left(\mathbf{s}^i_{A_2} + \mathbf{W}_{A_{22}}\mathbf{s}^i_{B_2}\right). \end{aligned} \tag{43}$$

The scattering equation for the combined block AB can now be determined by excluding the subvectors $\mathbf{v}^i_{A_2}$, $\mathbf{v}^r_{A_2}$, $\mathbf{v}^i_{B_2}$, and $\mathbf{v}^r_{B_2}$ from the consideration [23]

$$\begin{bmatrix} \mathbf{W}_{AB_{11}} & \mathbf{W}_{AB_{12}} \\ \mathbf{W}_{AB_{21}} & \mathbf{W}_{AB_{22}} \end{bmatrix} \begin{bmatrix} \mathbf{v}^i_{A_1} \\ \mathbf{v}^i_{B_1} \end{bmatrix} + \mathbf{s}^i_{AB} = \begin{bmatrix} \mathbf{v}^r_{A_1} \\ \mathbf{v}^r_{B_1} \end{bmatrix}, \quad \begin{matrix} \} \\ \} \end{matrix} \begin{matrix} N_A - k \\ N_B - k \end{matrix} \tag{44}$$

where

$$\begin{aligned} \mathbf{W}_{AB_{11}} &= \mathbf{W}_{A_{11}} + \mathbf{W}_{A_{12}} \left(\mathbf{I} - \mathbf{W}_{B_{22}}\mathbf{W}_{A_{22}}\right)^{-1} \mathbf{W}_{B_{22}}\mathbf{W}_{A_{21}} \\ \mathbf{W}_{AB_{12}} &= \mathbf{W}_{A_{12}} \left(\mathbf{I} - \mathbf{W}_{B_{22}}\mathbf{W}_{A_{22}}\right)^{-1} \mathbf{W}_{B_{21}} \\ \mathbf{W}_{AB_{21}} &= \mathbf{W}_{B_{12}} \left(\mathbf{I} - \mathbf{W}_{A_{22}}\mathbf{W}_{B_{22}}\right)^{-1} \mathbf{W}_{A_{21}} \\ \mathbf{W}_{AB_{22}} &= \mathbf{W}_{B_{11}} + \mathbf{W}_{B_{12}} \left(\mathbf{I} - \mathbf{W}_{A_{22}}\mathbf{W}_{B_{22}}\right)^{-1} \mathbf{W}_{A_{22}}\mathbf{W}_{B_{21}} \end{aligned} \tag{45}$$

and

$$\mathbf{s}^i_{AB} = \begin{bmatrix} \mathbf{s}^i_{A_1}\mathbf{W}_{A_{12}} \left(\mathbf{I} - \mathbf{W}_{B_{22}}\mathbf{W}_{A_{22}}\right)^{-1} \left(\mathbf{s}^i_{B_2} + \mathbf{W}_{B_{22}}\mathbf{s}^i_{A_2}\right) \\ \mathbf{s}^i_{B_1}\mathbf{W}_{B_{12}} \left(\mathbf{I} - \mathbf{W}_{A_{22}}\mathbf{W}_{B_{22}}\right)^{-1} \left(\mathbf{s}^i_{A_2} + \mathbf{W}_{A_{22}}\mathbf{s}^i_{B_2}\right) \end{bmatrix}. \tag{46}$$

In the MR-FDTLM implementation, the procedure described above in (40)–(46) is applied recursively (see [5]). In agreement with the notation introduced in [5], Eq. (45) can be identified as the *preprocessing phase*, while Eq. (46) and Eq. (43) correspond to the *upward phase* and the *downward phase*, respectively.

In the following section, we consider the computational complexity of the MR-FDTLM implementation.

3.2.4 Computational Complexity

It is assumed that the computational load associated with the MR-FDTLM implementation, as well as the memory needs are due to the operations defined in (43), (45), and (46). The following *worst-case* figures have been used for estimating the computational cost:

- Sum of two general $n \times p$–matrices: $O\{np\}$;
- Product of one $n \times p$– and one $p \times k$–matrices: $O\{npk\}$;
- Matrix inversion: $O\{n^3\}$.

The computational load caused by the matrix manipulations in (45) is determined as

$$O\{2k^3 - 2(N_A + N_B - 1)k^2 + (1 + 2N_AN_B - 2N_A - 2N_B + N_A^2 + N_B^2)k + \\ +(N_A^2 + N_B^2)\}. \quad (47)$$

Consequently, the computational load associated with (46) is estimated to be

$$O\{(N_A + N_B)k + N_A + N_B\}. \quad (48)$$

while the estimated computational cost of (43) is given by

$$O\{-2k^3 - (2 + N_A + N_B)k^2 + (2 + N_A + N_B)k\}. \quad (49)$$

In (47)–(49), we have utilized the fact that the scattering matrices $\mathbf{W}_A$ and $\mathbf{W}_B$ are symmetrical.

A particular interest for us represent the case when the two scattering matrices $\mathbf{W}_A$ and $\mathbf{W}_B$ are of the same size, i.e., $N_A = N_B = N$. Under this condition, assume for simplicity that the propagation environment is a cube with $M = 2^L$ SSCN nodes located along each edge[1]. Then, for each level $l = 0, \ldots, L-1$, we obtain by using (47)–(49) the following estimates of the computational costs $\mathcal{C}_p(l)$, $\mathcal{C}_u(l)$, $\mathcal{C}_d(l)$ associated with the *preprocessing phase*, the *upward phase*, and the *downward phase*, respectively,

$$\begin{aligned} \mathcal{C}_p(l) &= O\{186 \cdot 6^3 \cdot 2^{3l} M^3\} \\ \mathcal{C}_u(l) &= O\{32 \cdot 6^2 \cdot 2^l M^3\} \\ \mathcal{C}_d(l) &= O\{24 \cdot 6^3 \cdot 2^{3l} M^3\}. \end{aligned} \quad (50)$$

The results in (50) are illustrated in Fig. 4, where the computational load $\mathcal{C}_p(l)$ for the *preprocessing phase* at the level l is shown relative to the total computational load for the *preprocessing phase*. The total computational cost of the *preprocessing phase*, as well as the total computational costs for the *upward phase* and the *downward phase*, are estimated as

- *preprocessing phase*: $O\{27 \cdot 6^3 \cdot M^6\}$;
- *upward phase*: $O\{32 \cdot 6^2 \cdot M^4\}$;
- *downward phase*: $O\{4 \cdot 6^3 \cdot M^6\}$.

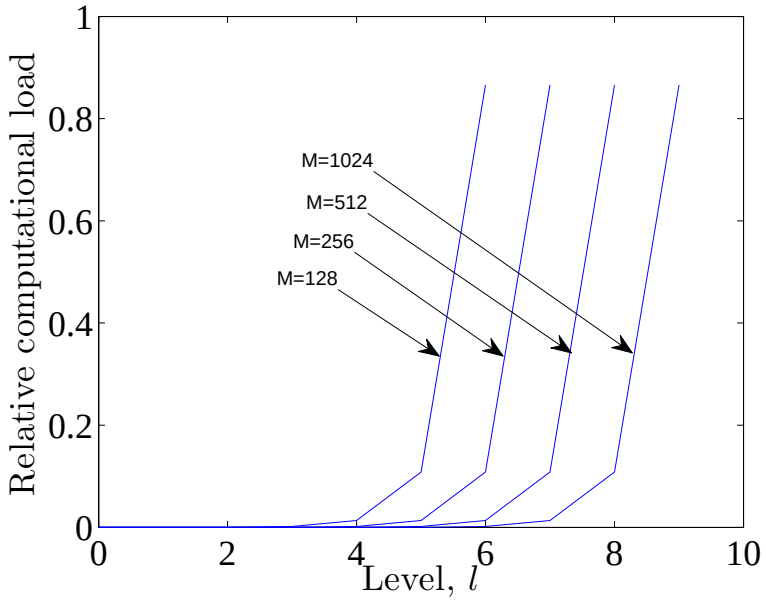

Figure 4: The computational load $\mathcal{C}_p(l)$ relative to the total computational load for the *preprocessing phase*.

Note that about 90% of the total estimated computational cost at the *preprocessing phase* is at the final L-th level.

Based on (43), (45), and (46), the memory needs can also be evaluated. It follows that the total required memory is estimated to be $O\{72 \cdot 6^2 \cdot M^4 \cdot mem\}$, where mem is the number of bytes required to store a complex variable.

The results presented above correspond to the case when the scattering matrices $\mathbf{W}_A$ and $\mathbf{W}_B$ that participate in the composition of scattering blocks (see Subsection 3.2.3) are of the same size. For comparison reasons, an alternative scenario can be considered, when on every iteration of the MR-FDTLM implementation (see Subsection 3.2.3), the matrix $\mathbf{W}_B$ represent the scattering matrix of a single SSCN node (25), i.e., $N_B = 12$. Without going into details, the upper bound for the total computational cost of the *preprocessing phase* is estimated in this case as $O\{490 \cdot M^7\}$.

In order to validate the advantage of using the MR-FDTLM implementation over the more traditional time domain implementation of the TLM method, the computational complexity of the latter has to be assessed. However, the computational load of the time-domain implementation cannot be easily estimated, due to the iterative nature of the algorithm and the dependence of the computational load on the desired accuracy. Therefore, in the following we assume that the simulation process in time domain must run for a number of iterations, which is as large as the volume of the simulated environment, i.e., M^3 for the scenario considered in this section (see also [24]). Under this assumption, the computation load for the time domain implementation of the TLM

[1]For example, $M = 1000$ corresponds to a cube with approximately 20 m edge length for the carrier frequency of 2.4 GHz

method, i.e., the reference computational cost, can be estimated as $O\{54 \cdot M^6\}$ (see Subsection 3.1.4).

It appears that the MR-FDTLM implementation can hardly be considered as a computationally efficient algorithm compared to the time domain implementation of the TLM method. However, the computational costs associated with the *preprocessing phase*, the *upward phase* and the *downward phase* shown above represent, in a manner of speaking, the worst case. Indeed, if instead of the *naive* approach to computing the matrix multiplications and inversions in (43), (45), and (46), we employ the Strassen fast matrix multiplication/inversion algorithms [25, 26], the following numbers for the total computational cost of the *preprocessing phase* and the *downward phase* can be obtained[2]

- *preprocessing phase*: $O\{161 \cdot 6^{2.8} \cdot M^{5.6}\}$;
- *downward phase*: $O\{39 \cdot 6^{2.8} \cdot M^{5.6}\}$.

These results are illustrated in Fig. 5, where the estimated total computational cost of the MR-FDTLM is shown relative to the reference computational cost. As can be seen from Fig. 5, the MR-FDTLM is computationally more

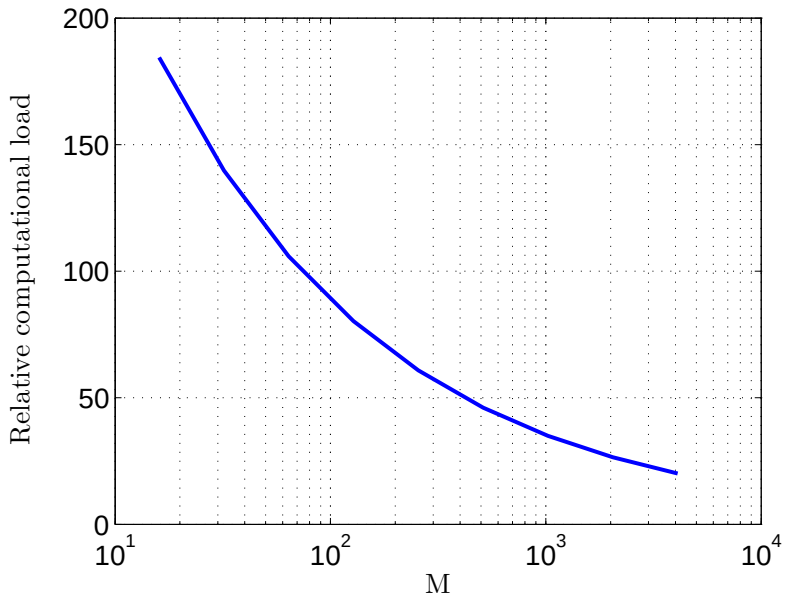

Figure 5: The the computational load of the MR-FDTLM relative to the the reference computational load.

efficient starting from $M \simeq 80$.

3.3 Multi-Frequency MR-FDTLM implementation

Let us again consider the matrix $\mathbf{W}^p(f)$ in (37). Suppose that the signal $\mathbf{v}^r(f_0)$ and the matrix $\mathbf{W}^p(f_0)$ corresponding to the frequency f_0 are known for each

[2]The total computational cost of the *upward phase* does not change.

node. Then, assuming that $\triangle f$ is sufficiently small, we can approximate the matrix $\mathbf{W}^p(f)$ at the frequency $f = f_0 + \triangle f$ as follows

$$\mathbf{W}^p(f) = \mathbf{W}^p(f_0) + \frac{d\mathbf{W}^p(f)}{df}|_{f=f_0} \triangle f = \mathbf{W}_0^p + \mathbf{W}_{\delta f}^p. \tag{51}$$

It can be shown that

$$\frac{d\mathbf{W}^p(f)}{df} = j2\pi \triangle t e^{j2\pi f \triangle t} \left(e^{j2\pi f \triangle t}\mathbf{I} - \mathbf{R}^p\right)^{-1} \mathbf{W}^p(f) \tag{52}$$

and

$$\mathbf{W}_{\delta f}^p = j2\pi \triangle t \triangle f e^{j2\pi f_0 \triangle t} \left(e^{j2\pi f_0 \triangle t}\mathbf{I} - \mathbf{R}^p\right)^{-1} \mathbf{W}_0^p. \tag{53}$$

The procedure developed in Section 2.3.2 can now be applied to efficiently calculate the signal $\mathbf{v}^r(f)$ at the frequency f from the known signal $\mathbf{v}^r(f_0)$.

4 Concluding Remarks

In this report, we have discussed three important contributions to adapt MR-FDPF to OFDM/MIMO systems. The first contribution concerns the estimation of a fading channel model, that was already presented in a previous paper [18]. We here improve this approach by considering an eigen decomposition of inward flows in an homogeneous receiving block. The second contribution is the extension to MIMO simulations by considering radiation patterns in source and reception blocks. The third contribution concerns wideband systems: MR-FDPF was optimized to compute a frequency domain impulse response. Then we derived a series based approximation to overcome the computational overload associated with a multiple harmonic approach.

We have also analyzed the possibility of applying the MR-FD approach to the TLM method in order to efficiently simulate the radio wave propagation in 3D indoor environments.

From the presented results, it follows that the 3D TLM scheme based on the SSCNs is a suitable candidate for the MR-FDTLM implementation. Indeed, only a few straightforward modifications of the scattering procedure implemented in the original MR-FDPF algorithm are required. More importantly, the preliminary analysis of the complexity of the MR-FDTLM implementation indicates a potential reduction in the computational load as compared to the more traditional time-domain realizations of the 3D TLM method.

Bibliography

[1] D. N. Schettino, F. J. S. Moreira, and C. G. Rego, "Efficient ray tracing for radio channel characterization of urban scenarios," *IEEE Trans. Magn.*, vol. 43, no. 4, pp. 1305–1308, 2007.

[2] G. Wolfle, B. E. Gschwendtner, and F. M. Landstorfer, "Intelligent ray tracing-a new approach for field strength prediction in microcells," in *Proc. IEEE 47th Vehicular Technology Conf*, vol. 2, 1997, pp. 790–794.

[3] A. Valcarce, G. D. L. Roche, Á. Jüttner, D. López-Pérez, and J. Zhang, "Applying FDTD to the coverage prediction of WiMAX femtocells," *EURASIP Journal on Wireless Communications and Networking*, vol. 2009, p. 13, 2009.

[4] M. Thiel and K. Sarabandi, "3d-wave propagation analysis of indoor wireless channels utilizing hybrid methods," *IEEE Trans. Antennas Propag.*, vol. 57, no. 5, pp. 1539–1546, 2009.

[5] J.-M. Gorce, K. Jaffres-Runser, and G. de la Roche, "Deterministic approach for fast simulations of indoor radio wave propagation," *IEEE Trans. Antennas Propag.*, vol. 55, no. 3, pp. 938–948, 2007.

[6] J.-M. Gorce, K. Jaffres-Runser, and G. D. L. Roche, "Deterministic approach for fast simulations of indoor radio wave propagation," *IEEE Transactions on Antennas and Propagation*, vol. 55, pp. 938–942, March 2007.

[7] G. de la Roche, K. Jaffres-Runser, and J.-M. Gorce, "On predicting in-building wiki coverage with a fast discrete approach," *International Journal of Mobile Network Design and Innovation*, vol. 2, pp. 3–12, 2007.

[8] G. de la Roche, G. Villemaud, and J.-M. Gorce, "Efficient finite difference method for simulating radio propagation in dense urban environments," Edimburgh, UK, 2007.

[9] G. de la Roche, P. Flipo, Z. Lai, G. Villemaud, J. Zhang, and J.-M. Gorce, "Combination of geometric and finite difference models for radio wave propagation in outdoor to indoor scenarios," Barcelona, Spain, 2010.

[10] B. Chopard, P. Luthi, and J. Wagen, "A lattice boltzmann method for wave propagation in urban microcells," in *IEEE Proceedings - Microwaves, Antennas and Propagation*, vol. 144, 1997, pp. 251–255.

[11] J. Zhang and G. de la Roche, *Femtocells: Technologies and Deployment*. John Wiley and Sons Ltd, 2010.

[12] S. Jing, D. N. C. Tse, J. B. Soriaga, J. Hou, J. E. Smee, and R. Padovani, "Multicell downlink capacity with coordinated processing," *EURASIP Journal on Wireless Comm. Networks*, vol. 2008, no. 5, pp. 1–19, 2008.

[13] A. Alsawah and I. Fijalkow, "Optimal frequency-reuse partitioning for ubiquitous coverage in cellular systems," in *15th European Signal Processing Conference (EUSIPCO)*, 2008.

[14] M. C. Necker, "Coordinated fractional frequency reuse," in *MSWiM'07: Proceedings of the 10th ACM Symposium on Modeling, analysis, and simulation of wireless and mobile systems*. New York, USA: ACM, 2007, pp. 296–305.

[15] G. De La Roche, X. Gallon, J.-M. Gorce, and G. Villemaud, "On predicting fast fading strength from Indoor 802.11 simulations," in *International Conference on Electromagnetics in Advanced Applications (ICEAA)*, IEEE, Ed., Torino Italie, 2007, pp. 407–410.

[16] J.-K. H. Juho Lee and J. C. Zhang, "Mimo technologies in 3gpp lte and lte-advanced," *EURASIP Journal on Wireless Communications and Networking*, 2009.

[17] "3GPP TR 25.996: Spatial channel model for multiple input multiple output (MIMO) simulations (Release 8)," December 2008.

[18] G. Villemaud, G. De La Roche, and J.-M. Gorce, "Accuracy Enhancement of a Multi-Resolution Indoor Propagation Simulation Tool by Radiation Pattern Synthesis," in *IEEE Antennas and Propagation Symposium*, Albuquerque États-Unis d'Amérique, 07 2006.

[19] "IEEE 802.16e-2005: Air interface for fixed and mobile broadband wireless access systems," 2005.

[20] B. Chopard and P. O. Luthi, "Lattice boltzmann computations and applications to physics," *Theor. Comput. Sci.*, vol. 217, no. 1, pp. 115–130, 1999.

[21] C. Christopoulos, *The Transmission-Line Modeling (TLM) Method in Electromagnetics*. Morgan & Claypool Publishers, 2006.

[22] V. Trenkic, "The development and characterization of advanced nodes for the TLM method," Ph.D. dissertation, University of Nottingham, 1995.

[23] V. V. Nikolsky and T. I. Nikolskaya, *Electrodynamics and Propagation of Radio Waves*. Moscow, Russia: Nauka, 1989, in Russian.

[24] J.-M. Gorce, K. Jaffrès Runser, and G. De La Roche, "The Adaptive Multi-Resolution Frequency-Domain ParFlow (MR-FDPF) Method for Indoor Radio Wave Propagation Simulation. Part I : Theory and Algorithms," INRIA, Tech. Rep. RR-5740, 11 2005. [Online]. Available: http://hal.inria.fr/inria-00070278/PDF/RR-5740.pdf

[25] J. R. Bunch and J. E. Hopcroft, "Triangular factorization and inversion by fast matrix multiplication," *Mathematics of Computation*, vol. 28, no. 125, pp. 231–236, Jan 1974. [Online]. Available: http://www.jstor.org/stable/2005828

[26] V. Pan, *How to multiply matrices faster*. New York, NY, USA: Springer-Verlag New York, Inc., 1984.